Contributions of aerosol composition and sources to particulate optical properties in a southern coastal city of China

Jie Tian, Qiyuan Wang, Yongming Han, Jianhuai Ye, Ping Wang, Siwatt Pongpiachan, Haiyan Ni, Yaqing Zhou, Meng Wang, Youzhi Zhao, Junji Cao

PII: S0169-8095(19)30793-8

DOI: https://doi.org/10.1016/j.atmosres.2019.104744

Reference: ATMOS 104744

To appear in: *Atmospheric Research*

Received date: 20 June 2019

Revised date: 4 October 2019

Accepted date: 3 November 2019

Please cite this article as: J. Tian, Q. Wang, Y. Han, et al., Contributions of aerosol composition and sources to particulate optical properties in a southern coastal city of China, *Atmospheric Research*(2018), https://doi.org/10.1016/j.atmosres.2019.104744

Contributions of aerosol composition and sources to particulate optical properties in a southern coastal city of China

Jie Tian[a,b,c], Qiyuan Wang[a,b,c*], Yongming Han[a,b], Jianhuai Ye[d], Ping Wang[e], Siwatt Pongpiachan[f], Haiyan Ni[a], Yaqing Zhou[a], Meng Wang[a], Youzhi Zhao[e], Junji Cao[a,b,c*]

[a]*Key Laboratory of Aerosol Chemistry & Physics, State Key Laboratory of Loess and Quaternary Geology, Institute of Earth Environment, Chinese Academy of Sciences, Xi'an 710061, China*

[b]*CAS Center for Excellence in Quaternary Science and Global Change，Xi'an 710061, China*

[c]*Shaanxi Key Laboratory of Atmospheric and Haze-fog Pollution Prevention, Xi'an 710061, China*

[d]*School of Engineering and Applied Sciences, Harvard University, Cambridge, Massachusetts, 02138 USA*

[e]*Hainan Tropical Ocean University, Sanya 572022, China*

[f]*School of Social & Environmental Development, National Institute of Development Administration (NIDA), Bangkok 10240, Thailand*

*Corresponding authors.

Tel.: +86-29- 62336205; Fax: +86-29-62336234

E-mail addresses: cao@loess.llqg.ac.cn (J. Cao) and wangqy@ieecas.cn (Q. Wang).

Abstract

The contributions of chemical composition and emission sources to aerosol optical properties were evaluated for a coastal city in southern China. The average dry light scattering coefficient ($b_{scat,dry}$) and light absorption coefficient (b_{abs}) were 32.5 ± 15.5 Mm^{-1} and 8.8 ± 4.7 Mm^{-1}, respectively. Diurnal cycles in $b_{scat,dry}$ and b_{abs} were observed with peak values in the morning and at night. Both $b_{scat,dry}$ and b_{abs} varied with wind speeds and directions, and thus affected by transport pathways. Chemical composition data for 12-hour $PM_{2.5}$ samples were used with the revised IMPROVE algorithm and a Hybrid Environmental Receptor Model to evaluate aerosol composition and source contributions to dry light extinction ($b_{ext,dry} = b_{scat,dry} + b_{abs}$), respectively. Ammonium sulfate and organic matter were the dominant contributors to $b_{ext,dry}$, followed by elemental carbon, sea salt, fine soil, and ammonium nitrate. The six $PM_{2.5}$ sources identified were secondary sulfate source, biomass burning, marine emission, fugitive dust, traffic-related emission, and shipping emission. Marine emission and secondary sulfate source were the largest contributors of $b_{ext,dry}$ during the daytime and nighttime, respectively. Backward trajectory analysis further explored the impact of potential sources to $b_{ext,dry}$ at Sanya from surrounding regions. The results of our study would be useful for improving models of radiative effects from different sources in this area.

Keywords: $PM_{2.5}$; Light extinction; Chemical composition; Source apportionment.

1. Introduction

With the rapid urbanization and economic growth in China over the past several decades, fine particulate matter ($PM_{2.5}$ with aerodynamic diameter ≤ 2.5 μm) has emerged as one of the most important pollutants because it impacts air quality, human health, and climate change on regional and global scales (Huang et al., 2014). Atmospheric aerosol can perturb the Earth's radiative balance directly by scattering and absorbing solar radiation and indirectly by acting as cloud condensation nuclei (Bellouin et al., 2013; Sekiguchi et al., 2003; Takemura et al., 2005). Due to the spatial and temporal variations of aerosol concentrations and composition, large uncertainties have been found in quantifying the direct and indirect effects of aerosol and the associated effects on estimating global radiative forcing (IPCC, 2013). To reduce these uncertainties, a thorough understanding of relationships of aerosol optical properties to chemical composition, microphysical properties, and probable sources is required at local, regional, even global scales. For example, the single scattering albedo (SSA), defined as the ratio of the light scattering coefficient (b_{scat}) to the light extinction coefficient (b_{ext}), is an important determinant in chemical transport models for computing radiative forcing. A small variation of SSA can change the estimated net direct radiative flux caused by the aerosol (Haywood and Boucher, 2000). Therefore, characterizing the atmospheric aerosol composition and understanding the relationships between emission sources and aerosol optical properties can provide a better information on how the aerosol affects atmospheric

radiative forcing and ultimately climate.

Aerosol b_{ext} is closely related to chemical composition (Watson, 2002), and the major aerosol components, including organic matter (OM), ammonium sulfate ($(NH_4)_2SO_4$), ammonium nitrate (NH_4NO_3), fine soil (FS), and sea salt (SS), have been considered as the most important contributors to b_{scat} (Moise et al., 2015). Elemental carbon (EC), on the other hand, is recognized as the main light-absorbing species (Bond et al., 2013). Cao et al. (2012) and Wang et al. (2016b) found that $(NH_4)_2SO_4$ and NH_4NO_3 were the main contributors (> 50%) to the annual b_{ext} for $PM_{2.5}$ in Xi'an and Chengdu, two mega inland cities in China. However, a recent study reported by Wang et al. (2015b) showed that OM, rather than inorganic aerosol, accounted for the major fraction (54%) of b_{scat} during winter in Beijing. Cui et al. (2016) found that NH_4NO_3 only accounted for 4.0% of total b_{ext} in suburban Nanjing. In addition, SS was found to account for as much as 13.7% of b_{ext} at Xiamen, a coastal city in southeastern China (Deng et al., 2016), suggesting the importance of SS in coastal areas. These results also indicate that the relative contributions of chemical species to b_{ext} vary strongly both geographically and temporally.

Receptor models have been commonly used to quantify the mass contributions of pollutants from different sources (Huang et al., 2014; Shi et al., 2009; Zhang et al., 2013), but only a few studies have used positive matrix factorization (PMF) and chemical mass balance (CMB) to identify and apportion the

potential sources for aerosol b_{ext} (Cao et al., 2012; Lan et al., 2018; Tao et al., 2014a; Wang et al., 2016d; Zhou et al., 2017). In one such study, Zhou et al. (2017) used PMF analysis to show that contributions of b_{ext} from sources including secondary aerosol, biomass burning, traffic-related emissions, and coal burning decreased during the controlled-period in Asia-Pacific Economic Cooperation (APEC) meeting in Beijing. Wang et al. (2016d) identified seven $PM_{2.5}$ sources through the use of a CMB model, and they showed that there were major contributions to b_{ext} from vehicle exhaust, secondary nitrate, and secondary sulfate.

Recently, intensive studies regarding $PM_{2.5}$ optical properties have been conducted in inland cities in China, including Xi'an, Nanjing, Beijing, and Chengdu (Cao et al., 2012; Cui et al., 2016; He et al., 2009; Jing et al., 2015; Wang et al., 2016b), but the related studies in coastal cities have been more limited (Deng et al., 2016; Tao et al., 2012; Xu et al., 2012b). Sanya, one of the most popular tourism destinations in China, is a typical coastal city which covers 1919.58 km^2 and has a population of ~7.6 million. The region around Sanya is subject to impacts from marine aerosols from the South China Sea and continental aerosols from Southeast Asia and East China. Therefore, it is an ideal place for exploring the effects of $PM_{2.5}$ chemical composition and sources on aerosol b_{ext} in a coastal environment. In this study, an intensive measurement campaign was conducted at Sanya, and the objectives were (1) to investigate the temporal and diurnal variations of b_{scat} and b_{abs}; (2) to examine the relationship between $PM_{2.5}$ chemical composition and b_{ext}; and (3)

to quantify the relative contributions of b_{ext} from different sources.

2. Methodology

2.1. Sampling site and period

Sanya is located in southern China (Figure S1), and its location makes it subject to the effects of Asian spring monsoon, which can facilitate the impact of biomass burning extending from Southeast Asian to the South China Sea and parts of southern China (Huang et al., 2013). To investigate this, aerosol optical properties were monitored at Sanya from April 12 to May 14, 2017. Measurements were taken from the rooftop of an administration building (~20 m above the ground level) at Hainan Tropical Ocean University (18° 18′ N, 109° 31′ E; Figure S2). The sampling site was located in a suburban district of Sanya (~10 km from the South China Sea), and it was surrounded by educational and residential districts with no intense industrial activities nearby.

2.2. Online measurements

In-situ aerosol b_{scat} and b_{abs} were measured simultaneously using a photoacoustic extinctiometer (PAX, Droplet Measurement Technology, Boulder, CO, USA) at a wavelength of 532 nm. The principles of the PAX have been described in detail elsewhere (Retama et al., 2015). Briefly, b_{scat} is measured in an aerosol scattering chamber with a wide-angle (5–175°) integrating reciprocal nephelometer, which responds to all particle types regardless of chemical composition, mixing state, and morphology. Intra-cavity photoacoustic technology is used to measure b_{abs} in an

acoustic chamber with a small sensitive microphone that responds to the pressure wave induced by the heating of light-absorbing particles. In this study, a PAX was operated with a $PM_{2.5}$ cyclone inlet to remove large particles. Air moisture and particle water was removed by a Nafion® dryer (MD-700-24S, Perma Pure, Inc., Lakewood, NJ, USA) before the particles entered the PAX. As shown in Figure S3, the ambient relative humidity (RH) decreased from 80.9 ± 12.1% to 52.1 ± 4.6% after drying. Ammonium sulfate and freshly generated propane soot were used to calibrate b_{scat} and b_{abs}, respectively, before and during the campaign period. Detailed description of PAX calibration can be found in Wang et al. (2018).

Meteorological parameters, including wind speed (WS), wind direction (WD), RH, and temperature (TEMP), were measured at 1-min resolution using an integrated automatic weather station (MAWS201, Vaisala, Helsinki, Finland).

2.3. $PM_{2.5}$ sample collection and analysis

A high-volume air sampler (TE-6070MFC, Tisch, Cleveland, OH, USA) was operated to collect $PM_{2.5}$ at a flow rate of 1.13 m^3 min^{-1}. A combined total of 68 $PM_{2.5}$ samples were collected during the daytime from 08:00 local stand time (LST – all time references that follow are given in LST) to 20:00 and the nighttime from 20:00 to 08:00 in the next day, including two field blanks. Samples were collected on quartz-fiber filters (Whatman QM/A, Clifton, NJ, USA) with 414 cm^2 deposition area. The quartz-fiber filters were pre-baked at 900 °C for 3 hours to remove trace organic compounds before sampling, and after sampling, they were stored in the

freezer at about –20 °C to avoid volatilization. The filters were weighed by a high precision electronic balance with a ± 1 μg sensitivity (ME 5-F, Sartorius, Göttingen, Germany) before and after sampling to determine the $PM_{2.5}$ mass.

Water-soluble inorganic ions (NO_3^-, SO_4^{2-}, Na^+, NH_4^+, K^+, and Mg^{2+}) were measured with an ion chromatograph (Dionex-600, Dionex Inc., Sunnyvale, CA, USA). Anions were determined using an IonPac AS14A column (8 mM Na_2CO_3/1 mM $NaHCO_3$ as the eluent), while cations were analyzed using an IonPacCS12A column (20 mM methanesulfonic acid as the eluent). Standard reference materials produced by the National Research Center for Certified Reference Materials (Beijing, China) were analyzed for quality control and assurance purposes. A suite of elements was analyzed by an energy-dispersive X-ray fluorescence (ED-XRF) spectrometry (PANalytical Epsilon 5, Almelo, The Netherlands), including Ca, Sc, Ti, V, Fe, Co, Zn, and Mo. Quality assurance of adopting quartz-fiber filter was guaranteed by comparisons of ED-XRF analysis for matched pairs of quartz-fiber filter and Teflon-membrane filter. Significant positive correlation with slopes closed to unity for most elements indicated that elemental data for the quartz-fiber filter were reliable in this study (Figure S4). More detailed descriptions of measurements for water-soluble ions and elements can be found in Zhang et al. (2011) and Xu et al. (2012a), respectively.

Carbonaceous aerosol including organic carbon (OC) and elemental carbon (EC) were analyzed using a Desert Research Institute (DRI) Model 2001

Thermal/Optical Carbon Analyzer (Atmoslytic Inc., Calabasas, CA, USA). The adopted IMPROVE_A thermal/optical reflectance (TOR) protocol defined temperature plateaus for thermally derived four OC fractions of 140 °C for OC1, 280 °C for OC2, 480 °C for OC3, and 580 °C for OC4 in a helium (He) carrier gas and three EC fractions of 580 °C for EC1, 740 °C for EC2, and 840 °C for EC3 in a 98% He/2% O_2 carrier gas. OC is calculated as the sum of four OC fractions and the pyrolyzed carbon fraction (OP), and EC is calculated as the sum of three EC fractions minus OP (Chow et al., 2007).

Hopanes, which are markers for traffic emissions, were detected and quantified for the filter samples using an in-injection port thermal desorption (TD) coupled with gas chromatography/mass spectrometry (GC/MS) (Agilent 7890/5975C-Gas Chromatography/Mass Spectrometer, Santa Clara, CA, USA). Compared with traditional method of solvent extraction using GC/MS, the TD-GC/MS method has advantages of less sample preparation time, minimized potential contamination, and lower detection limits. A detailed description of TD-GC/MS operation may be found in Wang et al. (2016c). In this study, Hopanes involve 17α(H)-21α(H)-hopane, 17α(H)-21β(H)-hopane, 17β(H)-21α(H)-hopane, 17α(H)-22, 29, 30-Trisnorhopane, 17α(H)-21β(H), 30-Norhopane, 17β(H)-21α(H), 30-Norhopane, 17α(H)-21β(H), (22S)-homohopane, and 17α(H)-21β(H), (22R)-homohopane.

For quality assurance and control, one replicate sample was analyzed for

every ten samples for each type of chemical analysis. The allowable relative standard deviations between duplicate results were set to < 10% for filter samples, and that can be considered a measure of analytical precision. Field blanks were analyzed to correct for possible background contamination during the sampling period. Therefore, the relative standard deviation of chemical specie x (RSD_x) can be obtained as follows:

$$RSD_x = \frac{\sum_{i=1}^{n} \frac{2 \times (|[x_i]_{r1} - [x_i]_{r2}|)}{[x_i]_{r1} + [x_i]_{r2} - 2 \times [x]_b}}{n} \quad \cdots\cdots(1)$$

where n is the number of samples submitted for replicate analysis; $[x_i]_{r1}$ and $[x_i]_{r2}$ are the mass concentrations of $PM_{2.5}$ component x in sample i from replicate analysis; $[x]_b$ is the average mass concentration of $PM_{2.5}$ component x in field blank samples.

2.4. Data analysis

The revised Interagency Monitoring of Protected Visual Environments (IMPROVE) algorithm (Malm and Hand, 2007) was used to estimate b_{ext}, as shown in equation (2) to (5).

$$b_{ext} = b_{scat} + b_{abs} \approx (2.2 \times f_S(RH) \times \left[(NH_4)_2SO_4\right]_{small} + 4.8 \times f_L(RH) \times \left[(NH_4)_2SO_4\right]_{large} + 2.4 \times f_S(RH) \times [NH_4NO_3]_{small} + 5.1 \times f_L(RH) \times [NH_4NO_3]_{large} + 2.8 \times [OM]_{small} + 6.1 \times [OM]_{large} + 1.7 \times f_{ss}(RH) \times [SS] + 1 \times [FS]) + (10 \times [EC]) \cdots\cdots(2)$$

$$[X]_{Large} = \frac{[X]^2}{20\ \mu g\ m^{-3}} \quad ([X] < 20\ \mu g\ m^{-3}) \cdots\cdots(3)$$

$$[X]_{Large} = [X] \quad ([X] \geq 20\ \mu g\ m^{-3}) \cdots\cdots (4)$$

$$[X]_{Small} = [X] - [X]_{Large} \quad \cdots\cdots(5)$$

where fixed parameters are dry mass scattering and absorption efficiencies of chemical species; The bracket notation [X] represents the concentration of $PM_{2.5}$ component X in μg m^{-3}; $[(NH_4)_2SO_4]$ and $[NH_4NO_3]$ were calculated from $1.375\times[SO_4^{2-}]$ and $1.29\times[NO_3^-]$, respectively (Chow et al., 2015). It should be noted that $(NH_4)_2SO_4$ concentration was overestimated in our study due to the existence of ammonium bisulfate (NH_4HSO_4) (Figure S5); [OM] and [SS] were estimated by multiplying the [OC] and $[Na^+]$ by factors of 1.6 and 3.1, respectively (Pitchford et al., 2007; Turpin and Lim, 2001); [FS] is the concentration of fine soil that was determined from Fe level ([Fe]/0.029) (CNEMC, 1990); The subscripts "small" and "large" denote chemical species concentration smaller than, or greater than, 20 μg m^{-3}, respectively; $PM_{2.5}$ contains hygroscopic species (e.g., sulfates and nitrates), which can enhance b_{scat} with increased RH (Liu et al., 2014), and in the equations above, $f_L(RH)$ and $f_S(RH)$ represent RH growth curves corresponding the large and small mode of $(NH_4)_2SO_4$ and NH_4NO_3, respectively; Similarly, $f_{ss}(RH)$ is the sea salt hygroscopic growth curve. The growth curves for each species were derived from Pitchford et al. (2007). Specially, more than 95% of hourly RHs measured by PAX with a Nafion® dryer was below 60%. b_{ext} and b_{scat} under dry condition ($b_{ext,dry}$ and $b_{scat,dry}$) can be reconstructed using the RH measured by the PAX after drying.

To further evaluate whether the determined chemical species can represent the measured $PM_{2.5}$, the $PM_{2.5}$ concentration was reconstructed by the sum of

$(NH_4)_2SO_4$, NH_4NO_3, OM, EC, SS, and FS concentrations. As shown in Figure S6, the reconstructed $PM_{2.5}$ concentrations were correlated strongly with those measured values (R^2 = 0.99, $p < 0.001$) with a slope of 1.08 ± 0.01. The result indicated that the above dominant chemical components could reliably account for the $PM_{2.5}$.

2.5. Receptor model for source apportionment

The Hybrid Environmental Receptor Model (HERM) was used to identify the sources for $b_{ext,dry}$. This is a new approach for air pollution source apportionment, which combines theory of effective-variance chemical mass balance (EV-CMB) and positive matrix factorization (PMF) models. Similar to other multivariate receptor models (e.g., CMB and PMF), the HERM decomposes the measured aerosol concentrations into factor profiles (F), source contributions (S), and residuals (e):

$$C_{ik} = \sum_{j=1}^{J} F_{ij} S_{jk} + e_{ik} \quad \cdots\cdots(6)$$

where C_{ik} is the measured concentration of the i^{th} species in the k^{th} sample; F_{ij} is the i^{th} species concentration in the j^{th} source; S_{jk} represents the contribution of the j^{th} source to the k^{th} sample; and e_{ik} is the model residuals of i^{th} species concentration in the k^{th} sample. Based on the iterative conjugate gradient algorithm, the HERM minimizes the reduced chi-square (x^2) by seeking the optimized F and S matrixes:

$$x^2 = \frac{1}{K(I-J) - \sum_{i=1}^{I}\sum_{j=1}^{J}\delta_{ij}} \sum_{k=1}^{K}\sum_{i=1}^{I} \frac{\left(C_{ik} - \sum_{j=1}^{J} F_{ij}S_{jk}\right)^2}{\sigma_{C_{ik}}^2 + \sum_{j=1}^{J}\left(\sigma_{F_{ij}}^2 S_{jk}^2 + \beta\delta_{ij}C_{ik}^2\right)} \quad \cdots\cdots(7)$$

where K, I, and J are the number of samples, species, and sources, respectively. δ_{ij} = 0 when factor profile species F_{ij} is specified, whereas δ_{ij} = 1 means that F_{ij} is

unknown. $\sigma_{C_{ik}}$ and $\sigma_{F_{ij}}$ are the uncertainty matrixes of aerosol concentrations and factor profiles, respectively. β is an adjustable factor with a default value of 1. The principles of the HERM have been discussed in detail in Chen and Cao (2018). Here, HERM version 1.8 was employed, and 17 chemical species in $PM_{2.5}$ (OC, EC, NO_3^-, SO_4^{2-}, Na^+, NH_4^+, K^+, Mg^{2+}, Ca, Sc, Ti, V, Fe, Co, Zn, Mo, and Hopanes (the sum of eight individual hopanes)) were input into the model. A range of solutions were examined with different number of factors (3–8), and six-factor was finally selected for discussion because it was the most physically interpretable.

To further investigate the contributions of $PM_{2.5}$ sources to $b_{ext,dry}$, a multiple linear regression (MLR) of measured $b_{ext,dry}$ versus the $PM_{2.5}$ mass concentration from six sources was conducted:

$$b_{ext,dry} = \sum_{i=1}^{6} a_i \times [Source_i] \quad \cdots\cdots(8)$$

where $b_{ext,dry}$ is given in units Mm^{-1} from the PAX measurement; a_i is representative of the mass extinction efficiency (MEE) of $PM_{2.5}$ from source i in $m^2\ g^{-1}$; [$Source_i$] is the $PM_{2.5}$ mass concentration from source i in $\mu g\ m^{-3}$. Finally, the total amount of $b_{ext,dry}$ can be estimated statistically using individual source $PM_{2.5}$ concentration and MEEs.

2.6. Back trajectory analysis

A GIS-based software TrajStat was utilized to characterize the atmospheric transport of aerosol to Sanya during the campaign period (Wang et al., 2009). The built-in Hybrid Single-Particle Lagrangian Integrated Trajectory (HYSPLIT) model

developed by the National Oceanic and Atmospheric Administration (NOAA) can calculate trajectories to determine the origin of air masses and establish source-receptor relationships (Draxler and Hess, 1998; Rolph et al., 2017; Stein et al., 2015). In this study, 66 three-day air-mass trajectories calculated backwards in time were obtained from 08:00 and 20:00 of starting times by using the gridded meteorological data from Global Data Assimilation System (GDAS). A cluster analysis was further performed on these back trajectories based on an angle distance statistics method, which classified the group of air masses depending on the similar direction (Text S1). More detailed description of cluster analysis can be found in Sirois and Bottenheim, (1995) and Wang et al. (2018). Furthermore, the source contributions to $b_{ext,dry}$ for the daytime and nighttime were matched to the trajectories from each cluster starting 08:00 and 20:00, respectively, and the potential impacts of regional source on particles' optical properties at Sanya were then evaluated.

3. Results and discussion

3.1. Aerosol optical properties

3.1.1. Temporal variations of $b_{scat,dry}$ and b_{abs}

Figure 1 illustrates the time series of hourly $b_{scat,dry}$ and b_{abs} during the whole sampling period, and a statistical summary of the data are shown in Table 1. Hourly $b_{scat,dry}$ and b_{abs} values varied by 40 folds from 2.7 Mm^{-1} to 107.8 Mm^{-1} and 28 folds from 1.2 Mm^{-1} to 33.9 Mm^{-1}, respectively, leading to SSA varying from 0.54 to 0.86.

Compared with $b_{scat,dry}$ and b_{abs} observed in previous studies (Table S1), the average $b_{scat,dry}$ (32.5 ± 15.5 Mm^{-1}) and b_{abs} (8.8 ± 4.7 Mm^{-1}) at Sanya was well below the range of values (185.9–525.3 Mm^{-1} for $b_{scat,dry}$ and 23.9–119 Mm^{-1} for b_{abs}) measured at inland sites of China (Cao et al., 2012; Cui et al., 2016; Gong et al., 2015; He et al., 2009; Jing et al., 2015; Li et al., 2007a; Tao et al., 2014a; Wang et al., 2016b; Zhou et al., 2017; Zhu et al., 2015). Moreover, both $b_{scat,dry}$ and b_{abs} at Sanya were obviously lower than those reported for other coastal cities of China (Deng et al., 2016; Han et al., 2015; Tao et al., 2012; Tao et al., 2014b; Wang et al., 2017; Xu et al., 2012b), but they were comparable to those measured at coastal sites around the Mediterranean Sea such as Finokalia (44.2 ± 17.5 Mm^{-1} for b_{scat} and 6.3 ± 2.7 for b_{abs}) and Corsica (30 ± 20 Mm^{-1} for b_{scat}) (Bryant et al., 2006; Claeys et al., 2017). The small values for $b_{scat,dry}$ and b_{abs} at Sanya were consistent with the low $PM_{2.5}$ loadings there: the average PM2.5 mass concentration of 14.3 ± 4.2 μg m^{-3} was about half of the China National Ambient Air Quality Grade I Standards (35 μg m^{-3}, GB3095-2012).

Diurnal variations in $b_{scat,dry}$, b_{abs}, wind speed, and mixed layer depth averaged over all data from the campaign are plotted in Figure 2. Both $b_{scat,dry}$ and b_{abs} exhibited a "two peaks and two valleys" pattern. Indeed, both variables started to increase in the early morning at ~06:00, and reached their first peak values (39.6 ± 17.3 Mm^{-1} for $b_{scat,dry}$ and 11.6 ± 3.4 Mm^{-1} for b_{abs}) around ~07:00–08:00. The peak shortly after sunrise can be likely attributed to emissions from motor vehicles

during the morning rush hours. After that, $b_{scat,dry}$ and b_{abs} decreased, and both reached their lowest values at ~13:00–14:00. On the one hand, the gradually increased mixed layer depth and wind speed (Figure 2c and d) could accelerate the diffusion of atmospheric aerosols resulting in the $b_{scat,dry}$ and b_{abs} decline (Quan et al., 2013); On the other hand, FS and SS associated with wind-blown dust and sea breeze might increase with wind speed (Table 1), and that would lead to the higher values for $b_{scat,dry}$. The combination of positive and negative effects eventually led to a smaller decrease in $b_{scat,dry}$ relative to b_{abs} in the afternoon. After sunset, as mixed layer depth became shallow (< 360 m) and wind speed decreased ~0.20 m s^{-1}, pollutants emitted by anthropogenic sources (e.g., traffic in the evening rush hours and cooking activities) were trapped near the surface, leading to an increasing trend of $b_{scat,dry}$ and b_{abs} around 19:00–21:00. Thereafter, $b_{scat,dry}$ and b_{abs} showed a decreasing trend until 03:00, which may be attributed to the gradually decreased anthropogenic activities at night.

3.1.2. Influence of the meteorological conditions on $b_{scat,dry}$ and b_{abs}

Figure S7 shows the wind speeds and directions during the daytime and the nighttime over the sampling period. Overall, stagnant weather system occurred frequently; that is, > 80% of the wind speeds were lower than 1.0 m s^{-1}. The average wind speed was 0.78 ± 0.62 m s^{-1} during the daytime with higher wind speeds often associated with westerly, southwesterly, and easterly flows. In contrast, the average wind speed was just 0.19 ± 0.34 m s^{-1} during the nighttime with high values (> 1.0 m

s^{-1}) mostly related to easterly flow.

To investigate the potential for the horizontal advection of $b_{scat,dry}$ and b_{abs}, we further established the relationships between aerosol optical coefficients and wind speed and wind direction using bivariate polar plots (Figure 3) (Carslaw and Beevers, 2013). During the daytime (Figure 3a and b), b_{abs} appeared to have a stronger association with local sources (e.g., traffic emission) since high values tended to occur mostly at slow wind speed (< 1.0 m s^{-1}). This is reasonable because stable meteorological condition would favor the accumulation of locally-generated pollutants. Compared with b_{abs}, the polar plot of $b_{scat,dry}$ showed more dispersed feature, indicating that $b_{scat,dry}$ had relatively larger contributions from regional sources. For wind speeds > 1.0 m s^{-1}, high daytime $b_{scat,dry}$ values were associated with airflow from the northwest, southwest, and east, and that was likely due to the transport of scattering chemical species, especially FS and SS from up-wind regions in those directions. In contrast, low values for b_{abs} were observed under high-speed wind, and that was probably because there were relatively weak EC sources upwind, and strong winds would tend to disperse b_{abs}. During the nighttime (Figure 3c and d), high $b_{scat,dry}$ and b_{abs} values were related to the airflow from northeast when wind speeds exceeded 1.0 m s^{-1}. That may be an indication that aerosols were transported from eastern coastal regions of inland China (Zhou et al., 2018).

3.2. Contributions of chemical composition to aerosol optical properties

To identify the contributions of specific $PM_{2.5}$ chemical component to light

extinction of aerosols, optical coefficients ($b_{scat,dry}$, b_{abs}, and $b_{ext,dry}$) were reconstructed using the revised IMPROVE algorithm. The $b_{scat,dry}$, b_{abs}, and $b_{ext,dry}$ measured by PAX showed strong correlations (R^2 = 0.70–0.81) with those reconstructed by IMPROVE algorithm (Figure S8 and Figure 4a), and the slopes of linear regressions were close to unity (0.89–1.27), suggesting that the IMPROVE algorithm was a reasonable way of estimating the aerosol optical parameters at Sanya during the sampling period. We noted that the bias between the reconstructed and measured optical parameters were likely due to the lack of locally-derived dry scattering and absorption coefficients of chemical composition.

As shown in Figure 4b, chemical composition apportionment revealed that $(NH_4)_2SO_4$ and OM were the dominant contributors to $b_{ext,dry}$, accounting for 34.5 ± 8.6% and 23.6 ± 7.0%, respectively. This result is in agreement with recent measurements made at other coastal cities in China (e.g., Guangzhou and Xiamen) (Deng et al., 2016; Tao et al., 2014b). Furthermore, $b_{ext,dry}$ from $(NH_4)_2SO_4$ and OM during the daytime (16.6 ± 5.5 Mm^{-1} and 12.0 ± 4.8 Mm^{-1}) were similar to those during the nighttime (18.9 ± 7.4 Mm^{-1} and 12.0 ± 4.8 Mm^{-1}), which is due to small change of their mass concentrations (Table 1). In contrast, $b_{ext,dry}$ from EC, SS, and FS showed obvious daytime-nighttime variations. The average contribution of EC to $b_{ext,dry}$ was 15.3 ± 3.6%, with larger value at nighttime (8.6 ± 2.8 Mm^{-1}) than the daytime (6.9 ± 2.4 Mm^{-1}). This may be due to the intensive traffic in the evening combined with the low mixed layer depth. As a typical chemical composition of

aerosol in the coastal region, the contribution of SS to $b_{ext,dry}$ (12.0 ± 4.7%) cannot be ignored. $b_{ext,dry}$ from SS and FS had higher values for the daytime than for the nighttime. High wind speed during the daytime can lead to the high FS and SS concentrations associated with wind-blown dust and sea breeze, and that could help explain the above daytime/nighttime difference in $b_{ext,dry}$. Previous studies reported that NH_4NO_3 was an important aerosol particle for light extinction (Pitchford et al., 2007), but its contribution at Sanya was less than 10.0% (6.2 ± 2.1%), which was much lower than inland cities in China, e.g., Xi'an (23.1%, Cao et al., 2012), Chengdu (20.1–28.1%, Wang et al., 2016b), and Beijing (16–19%, Zhou et al., 2017), where NO_x emissions were strong (Diao et al., 2018; Zhang et al., 2007).

3.3. Source apportionment of aerosol optical properties

The HERM model was employed to apportion $b_{ext,dry}$ to source factors. The chemical species in $PM_{2.5}$, including OC, EC, NO_3^-, SO_4^{2-}, Na^+, NH_4^+, K^+, Mg^{2+}, Ca, Sc, Ti, V, Fe, Co, Zn, Mo, and Hopanes were used as model inputs. Numerous runs of HERM were performed, and in the end, six presumptive sources were identified, including secondary sulfate source, biomass burning, marine emission, fugitive dust, traffic-related emission, and shipping emission. The results obtained with the HERM model were used in a MLR to estimate each source contribution to $b_{ext,dry}$, and Figure 5 shows the source-factor profiles.

Factor 1 was most heavily loaded with SO_4^{2-} (45%) and NH_4^+ (71%), which were typically related with secondary particle formations (Liu et al., 2017; Wang et

al., 2016a), and therefore, this factor was identified as the secondary sulfate source. Factor 2 was enriched in K^+ (54%), which is an indicator of crop residue and wood burning (Li et al., 2007b; Ni et al., 2017), and this factor was assigned to biomass burning. Factor 3 was identified as marine emission because it had high loadings of Na^+ (41%), Mg^{2+} (58%), Ca (28%), and NO_3^- (38%), which are associated with fresh and aged sea-salt (Viana et al., 2015). Factor 4 was defined as fugitive dust, which included high levels of Ca (62%), Ti (79%), and Fe (62%) (Wang et al., 2015a). Factor 5 was characterized by high loadings of OC (38%), EC (30%), Hopanes (29%), and Zn (50%), and it was classified as traffic-related emissions. In fact, Hopanes can be considered as a fingerprint species for traffic emission (Mancilla et al., 2015), and OC and EC together are well related to traffic emissions (Chow et al., 2004; Liu et al., 2017). Additionally, Zn could be derived from brake linings and tires of vehicles (Song et al., 2006). Factor 6 was categorized as shipping emission, which has high loadings of V (59%), Hopanes (55%), OC (24%), and EC (24%). This corroborated the shipping emission origin of this factor, as V is a well-known tracer of crude oil burning (Manousakas et al., 2017).

As shown in Figure 6a, the predicted $b_{ext,dry}$ ($b_{ext,dry}$-predicted) based on the combination of HERM and MLR method was correlated strongly ($R^2 = 0.71$, $p < 0.001$) with those measured by the PAX. Moreover, the slope of 0.98 ± 0.02 indicated a reasonable performance of using source apportionment. Even so, $b_{ext,dry}$-predicted was slightly underestimated, and that was due to some residual

$PM_{2.5}$ that was not apportioned by the HERM. Figure 6b shows the relative contributions of each identified source to the predicted $b_{ext,dry}$, and clear differences in source contribution to $b_{ext,dry}$ during the daytime and the nighttime were evident. Of the six source categories, marine emission was found to be the most important contributor during the daytime accounting for 32.9 ± 19.5% of $b_{ext,dry}$, followed by biomass burning (19.0 ± 19.6%), secondary sulfate source (16.3 ± 4.0%), fugitive dust (16.2 ± 4.0%), traffic-related emission (11.9 ± 9.2%), and shipping emission (3.7 ± 2.6%). In contrast, the contribution of marine emission decreased to 10.5 ± 9.5% of $b_{ext,dry}$ during the nighttime. This was in accordance with the influences of sea breeze during the daytime whereas land breeze during the nighttime. Secondary sulfate source became the largest contributor (39.0 ± 14.6%) to $b_{ext,dry}$ during the nighttime, and that may have been related chemical processing. It is possible that the sulfate particles were aged at night with larger size compared with fresh one during the daytime (Lin et al., 2014). Biofuels are an important residential energy for local activities, and that is likely reason that the contribution of biomass burning increased to 27.9 ± 9.9% of $b_{ext,dry}$ during the nighttime. The contribution of fugitive dust was small (2.5 ± 2.0%) to $b_{ext,dry}$ presumably due to limited construction activities at night. Traffic-related emission (14.1 ± 10.7%) and shipping emission (6.0 ± 3.8%) had similar contributions to $b_{ext,dry}$ during the nighttime and the daytime.

3.4. Influence of regional transport on aerosol optical properties

Backward air mass trajectories were grouped into clusters and used to investigate the impact of regional transport on $b_{ext,dry}$. Figure 7 shows the map of four cluster-mean trajectories during the entire campaign period. The air masses associated with Cluster #1 originated from the South China Sea near Indochina Peninsula, and the average $b_{ext,dry}$ was 43.6 ± 10.7 Mm^{-1}. About 44% of trajectories were collocated to Cluster #2, which originated from the South China Sea with the lowest average $b_{ext,dry}$ (34.2 ± 8.2 Mm^{-1}) of the four clusters. Cluster #3 had the longest moving trajectory originating from eastern coastal regions in inland China, and this cluster had $b_{ext,dry}$ of 49.5 ± 14.7 Mm^{-1}. The air masses grouped into Cluster #4 derived from Thailand, Laos, and Vietnam. Although Cluster #4 had only 4 trajectories, the air masses from this cluster were associated with the highest $b_{ext,dry}$ (57.3 ± 11.6 Mm^{-1}). As shown in pie charts of Figure 7, secondary sulfate source was the dominant contributor to $b_{ext,dry}$ for all clusters. High contribution of biomass burning to $b_{ext,dry}$ was found for Cluster #1 and #4. Previous studies have shown that biomass burning is strong in Southeast Asia (Fu et al., 2011; Huang et al., 2013), and this is supported by Figure S9 which shows that a large number of fire counts were observed in Southeast Asia during the sampling period. Cluster #2 had the largest contribution from marine emission to $b_{ext,dry}$, and shipping emission contribution was also the highest in four clusters. The largest contribution of traffic-related emission to $b_{ext,dry}$ was associated with Cluster #3, and this was

consistent with heavy traffics in southeastern coastal cities of China (Wang et al., 2012).

4. Conclusion

Online measurements of dry light scattering coefficient ($b_{scat,dry}$) and light absorption coefficient (b_{abs}) were conducted together with analyses of $PM_{2.5}$ composition at Sanya, a southern coastal city of China, from April 12 to May 14, 2017. The $b_{scat,dry}$ and b_{abs} grand averages for the entire campaign were 32.5 ± 15.5 Mm^{-1} and 8.8 ± 4.7 Mm^{-1}, respectively, and they were relatively low compared with values reported for inland sites in China, which is consistent with the low $PM_{2.5}$ loadings at Sanya (14.3 ± 4.2 μg m^{-3}). Diurnal variations in $b_{scat,dry}$ and b_{abs} were observed with a pattern of "two peaks and two valleys" as a result of combined effects from anthropogenic sources emission and meteorological conditions. Bivariate polar plots showed that $b_{scat,dry}$ had more dispersed feature compared to b_{abs} during the daytime, indicating that more $b_{scat,dry}$ contribution was attributed to regional sources from the northwest, southwest, and east, while b_{abs} was more strongly influenced by local sources. Both of $b_{scat,dry}$ and b_{abs} were largest in northeast wind during the nighttime.

The contributions of chemical composition and sources to aerosol extinction under dry condition ($b_{ext,dry}$) were obtained using the revised IMPROVE algorithm and a Hybrid Environmental Receptor Model (HERM) combined with multiple linear regression (MLR), respectively. Chemical composition apportionment

revealed that ammonium sulfate and organic matter were the dominant contributors to $b_{ext,dry}$, accounting for 34.5 ± 8.6% and 23.6 ± 7.0%, respectively, followed by elemental carbon (15.3 ± 3.6%), sea salt (12.0 ± 4.7%), fine soil (8.4 ± 4.9%), and ammonium nitrate (6.2 ± 2.1%). Additionally, source apportionment further showed that $b_{ext,dry}$ was dominantly contributed by marine emission (32.9 ± 19.5%), followed by biomass burning (19.0 ± 19.6%), secondary sulfate source (16.3 ± 4.0%), fugitive dust (16.2 ± 4.0%), traffic-related emission (11.9 ± 9.2%), and shipping emission (3.7 ± 2.6%) during the daytime. In contrast, secondary sulfate source (39.0 ± 14.6%), biomass burning (27.9 ± 9.9%), and traffic-related emission (14.1 ± 10.7%) became the largest contributor to $b_{ext,dry}$ during the nighttime. The results provides insight into chemical composition and emission sources associated with aerosol extinction at Sanya, and should be useful for improving models of the radiative effects of specific chemical species and sources in this area.

Moreover, backward trajectory analysis indicated that biomass burning in Southeast Asia had a strong effect on $b_{ext,dry}$, while $b_{ext,dry}$ was dominated by traffic-related emission associated with transport from eastern coastal regions in inland China. These findings have important implications for the development of policies designed to control the main primary sources (e.g., biomass burning and traffic emission) at Sanya and surrounding regions. Biomass burning emissions and those from motor vehicles would appear to be a high priority for pollution control,

but the impact of transport from surrounding regions on aerosol populations and $b_{ext,dry}$ also need to be taken into account.

Acknowledgments

The authors declare no real or perceived financial conflicts of interests. This work was jointly supported by the National Natural Science Foundation of China (41661144020 and 41705106), the Key Research and Development Program of Shaanxi Province (2018-ZDXM3-01), the China Postdoctoral Science Foundation (2018M633523 and 2015M580890), and the Chinese Academy of Sciences (KLACP1703 and SKLLQG1529). Qiyuan Wang also acknowledged the support of the Youth Innovation Promotion Association, Chinese Academy of Sciences (2019402).

References

Bellouin, N., Quaas, J., Morcrette, J.J., Boucher, O., 2013. Estimates of aerosol radiative forcing from the MACC re-analysis. Atmos. Chem. Phys. 13, 2045-2062. https://doi.org/10.5194/acp-13-2045-2013

Bond, T.C., Doherty, S.J., Fahey, D.W., Forster, P.M., Berntsen, T., DeAngelo, B.J., Flanner, M.G., Ghan, S., Kärcher, B., Koch, D., Kinne, S., Kondo, Y., Quinn, P.K., Sarofim, M.C., Schultz, M.G., Schulz, M., Venkataraman, C., Zhang, H., Zhang, S., Bellouin, N., Guttikunda, S.K., Hopke, P.K., Jacobson, M.Z., Kaiser, J.W., Klimont, Z., Lohmann, U., Schwarz, J.P., Shindell, D., Storelvmo, T., Warren, S.G., Zender, C.S., 2013. Bounding the role of black carbon in the climate system: a scientific assessment. J. Geophys. Res.-Atmos. 118, 5380-5552. https://doi.org/10.1002/jgrd.50171

Bryant, C., Eleftheriadis, K., Smolik, J., Zdimal, V., Mihalopoulos, N., Colbeck, I., 2006. Optical properties of aerosols over the eastern Mediterranean. Atmos. Environ. 40, 6229-6244. https://doi.org/10.1016/j.atmosenv.2005.06.009

Cao, J.J., Wang, Q.Y., Chow, J.C., Watson, J.G., Tie, X.X., Shen, Z.X., Wang, P., An, Z.S., 2012. Impacts of aerosol compositions on visibility impairment in Xi'an, China. Atmos. Environ. 59, 559-566. https://doi.org/10.1016/j.atmosenv.2012.05.036

Carslaw, D.C., Beevers, S.D., 2013. Characterising and understanding emission sources using bivariate polar plots and k-means clustering. Environ. Modell. Softw. 40, 325-329. https://doi:10.1016/j.envsoft.2012.09.005

Chen, L-W.A., Cao, J.J., 2018. $PM_{2.5}$ source apportionment using a hybrid environmental receptor model. Environ. Sci. Technol. 52 (11), 6357-6369. https://doi.org/10.1021/acs.est.8b00131

Chow, J.C., Lowenthal, D.H., Chen, L.-W.A., Wang, X., Watson, J.G., 2015. Mass reconstruction methods for $PM_{2.5}$: a review. Air Qual. Atmos. Health. 8, 243-263. https://doi.org/10.1007/s11869-015-0338-3

Chow, J.C., Watson, J.G., Chen, L-W.A., Chang, M.O., Robinson, N.F., Trimble, D., Kohl, S., 2007. The IMPROVE_A temperature protocol for thermal/optical carbon analysis: maintaining consistency with a long-term database. J. Air Waste Manage. Assoc. 57, 1014-1023. https://doi.org/10.3155/1047-3289.57.9.1014

Chow, J.C., Watson, J.G., Kuhns, H., Etyemezian, V., Lowenthal, D.H., Crow, D., Kohl, S.D., Engelbrecht, J.P., Green, M.C., 2004. Source profiles for industrial, mobile, and area sources in the Big Bend Regional Aerosol Visibility and Observational study. Chemosphere. 54, 185-208. https://doi.org/10.1016/j.chemosphere.2003.07.004

Claeys, M., Roberts, G., Mallet, M., Arndt, J., Sellegri, K., Sciare, J., Wenger, J., Sauvage, B., 2017. Optical, physical and chemical properties of aerosols

transported to a coastal site in the Western Mediterranean: a focus on primary marine aerosols. Atmos. Chem. Phys. 17, 7891-7915. https://doi.org/10.5194/acp-17-7891-2017

China National Environmental Monitoring Centre (CNEMC), 1990. Background values of soil elements in China. Chinese Environmental Press, Beijing (in Chinese).

Cui, F., Chen, M., Ma, Y., Zheng, J., Yao, L., Zhou, Y., 2016. Optical properties and chemical apportionment of summertime $PM_{2.5}$ in the suburb of Nanjing. J. Atmos. Chem. 73, 119-135. https://doi.org/10.1007/s10874-015-9313-5

Deng, J., Zhang, Y., Hong, Y., Xu, L., Chen, Y., Du, W., Shen, J., 2016. Optical properties of $PM_{2.5}$ and the impacts of chemical compositions in the coastal city Xiamen in China. Sci. Total Environ. 557-558, 665-675. https://doi.org/10.1016/j.scitotenv.2016.03.143

Diao, B., Ding, L., Su, P., Cheng, J., 2018. The spatial-temporal characteristics and influential factors of NO_x emissions in China: a spatial econometric analysis. Int. J. Environ. Res. Public Health. 15, 1405. https://doi.org/10.3390/ijerph15071405

Draxler, R.R., Hess, G.D., 1998. An overview of the HYSPLIT_4 modelling system for trajectories, dispersion, and deposition. Aust. Meteor. Mag. 47, 295-308.

Fu, J.S., Hsu, N.C., Gao, Y., Huang, K., Li, C., Lin, N.H., Tsay, S.C., 2006. A regional chemical transport modeling to identify the influences of biomass

burning during 2006 BASE-ASIA. Atmos. Chem. Phys. Discuss. 11, 3071-3115. https://doi.org/10.5194/acpd-11-3071-2011

Gong, W., Zhang, M., Han, G., Ma, X., Zhu, Z., 2015. An investigation of aerosol scattering and absorption properties in Wuhan, central China. Atmosphere. 6, 503-520. https://doi.org/10.3390/atmos6040503

Han, T.T., Qiao, L.P., Zhou, M., Qu, Y., Du, J.F., Liu, X.G., Lou, S.R., Chen, C.H., Wang, H.L., Zhang, F., Yu, Q., Wu, Q., 2015. Chemical and optical properties of aerosols and their interrelationship in winter in the megacity Shanghai of China. J. Environ. Sci. 27, 59-69. https://doi.org/10.1016/j.jes.2014.04.018

Haywood, J., Boucher, O., 2000. Estimates of the direct and indirect radiative forcing due to tropospheric aerosols: a review. Rev. Geophys. 38, 513-543. https://doi.org/10.1029/1999rg000078

He, X., Li, C.C., Lau, A.K.H., Deng, Z.Z., Mao, J.T., Wang, M.H., Liu, X.Y., 2009. An intensive study of aerosol optical properties in Beijing urban area. Atmos. Chem. Phys. 9, 8903-8915. https://doi.org/10.5194/acpd-9-11413-2009

Huang, K., Fu, J.S., Hsu, N.C., Gao, Y., Dong, X., Tsay, S.C., Lam, Y.F., 2013. Impact assessment of biomass burning on air quality in Southeast and East Asia during BASE-ASIA. Atmos. Environ. 78, 291-302. https://doi.org/10.1016/j.atmosenv.2012.03.048

Huang, R.J., Zhang, Y., Bozzetti, C., Ho, K.F., Cao, J.J., Han, Y., Daellenbach, K.R., Slowik, J.G., Platt, S.M., Canonaco, F., Zotter, P., Wolf, R., Pieber, S.M., Bruns, E.A., Crippa, M., Ciarelli, G, Piazzalunga, A., Schwikowski, M., Abbaszade, G., Schnelle-Kreis, J., Zimmermann, R., An, Z., Szidat, S., Baltensperger, U., Haddad, I.E., Prévôt, A.S.H., 2014. High secondary aerosol contribution to particulate pollution during haze events in China. Nature. 514, 218-222. https://doi.org/ 10.1038/nature13774

IPCC., 2013. Climate Change 2013: The Physical Science Basis. Contribution of Working Group I to the Fifth Assessment Reprot of the Intergovemental Panel on Climate Change [Stocker, T.F., D. Qin, G.-K. Plattner, M. Tignor, S.K. Allen, J. Boschung, A. Nauels, Y. Xia, V. Bex and P.M. Midgley (eds.)]. Cambridage University Press, Cambrigde, United Kingdom and New York, NY, USA, 1535pp.

Jing, J., Wu, Y., Tao, J., Che, H., Xia, X., Zhang, X., Yan, P., Zhao, D., Zhang, L., 2015. Observation and analysis of near-surface atmospheric aerosol optical properties in urban Beijing. Particuology. 18, 144-154. https://doi.org/10.1016/j.partic.2014.03.013

Lan, Z., Zhang, B., Huang, X., Zhu, Q., Yuan, J., Zeng, L., Hu, M., He, L., 2018. Source apportionment of $PM_{2.5}$ light extinction in an urban atmosphere in China. J. Environ. Sci. 63, 277-284. https://doi.org/10.1016/j.jes.2017.07.016

Li, C., Marufu, L.T., Dickerson, R.R., Li, Z., Wen, T., Wang, Y., Wang, P., Chen, H., Stehr, J.W., 2007a. In situ measurements of trace gases and aerosol optical properties at a rural site in northern China during East Asian Study of Tropospheric Aerosols: an International Regional Experiment 2005. J. Geophys. Res.-Atmos. 112, D22S04. https://doi.org/10.1029/2006JD007592

Li, X., Wang, S., Duan, L., Hao, J., Li, C., Chen, Y., Yang, L., 2007b. Particulate and trace gas emissions from open burning of wheat straw and corn stover in China. Environ. Sci. Technol. 41, 6052-6058. https://doi.org/10.1021/es0705137

Lin, Z.J., Zhang, Z.S., Zhang, L., Tao, J., Zhang, R.J., Cao, J.J., Fan, S.J., Zhang, Y.H., 2014. An alternative method for estimating hygroscopic growth factor of aerosol light-scattering coefficient: a case study in an urban area of Guangzhou, South China. Atmos. Chem. Phys. 14, 7631-7644. https://doi.org/10.5194/acp-14-7631-2014

Liu, B., Wu, J., Zhang, J., Wang, L., Yang, J., Liang, D., Dai, Q., Bi, X., Feng, Y., Zhang, Y., Zhang, Q., 2017. Characterization and source apportionment of $PM_{2.5}$ based on error estimation from EPA PMF 5.0 model at a medium city in China. Environ. Pollut. 222, 10-22. https://doi.org/10.1016/j.envpol.2017.01.005

Liu, H.J., Zhao, C.S., Nekat, B., Ma, N., Wiedensohler, A., van Pinxteren, D., Spindler, G., Müller, K., Herrmann, H., 2014. Aerosol hygroscopicity

derived from size-segregated chemical composition and its parameterization in the North China Plain. Atmos. Chem. Phys.14, 2525-2539. https://doi.org/10.5194/acp-14-2525-2014

Malm, W.C., Hand, J.L., 2007. An examination of the physical and optical properties of aerosols collected in the IMPROVE program. Atmos. Environ. 41, 3407-3427. https://doi.org/10.1016/j.atmosenv.2006.12.012

Mancilla, Y., Mendoza, A., Fraser, M.P., Herckes, P., 2015. Chemical characterization of fine organic aerosol for source apportionment at Monterrey, Mexico. Atmos. Chem. Phys. Discuss. 15, 17967-18010. https://doi.org/10.5194/acpd-15-17967-2015

Manousakas, M., Papaefthymiou, H., Diapouli, E., Migliori, A., Karydas, A.G., Bogdanovic-Radovic, I., Eleftheriadis, K., 2017. Assessment of $PM_{2.5}$ sources and their corresponding level of uncertainty in a coastal urban area using EPA PMF 5.0 enhanced diagnostics. Sci. Total Environ. 574, 155-164. https://doi.org/10.1016/j.scitotenv.2016.09.047

Moise, T., Flores, J.M., Rudich, Y., 2015. Optical properties of secondary organic aerosols and their changes by chemical processes. Chem. Rev. 115, 4400-4439. https://doi.org/10.1021/cr5005259

Ni, H., Tian, J., Wang, X., Wang, Q., Han, Y., Cao, J., Long, X., Chen, L-W.A., Chow, J.C., Watson, J.G., Huang, R.J., Dusek, U., 2017. $PM_{2.5}$ emissions and

source profiles from open burning of crop residues. Atmos. Environ. 169, 229-237. https://doi.org/10.1016/j.atmosenv.2017.08.063

Pitchford, M., Maim, W., Schichtel, B., Kumar, N., Lowenthal, D., Hand, J., 2007. Revised algorithm for estimating light extinction from IMPROVE particle speciation data. J. Air Waste Manage. Assoc. 57, 1326-1336. https://doi.org/10.3155/1047-3289.57.11.1326

Quan, J., Gao, Y., Zhang, Q., Tie, X., Cao, J., Han, S., Meng, J., Chen, P., Zhao, D., 2013. Evolution of planetary boundary layer under different weather conditions, and its impact on aerosol concentrations. Particuology. 11, 34-40. https://doi.org/10.1016/j.partic.2012.04.005

Retama, A., Baumgardner, D., Raga, G.B., Mcmeeking, G.R., Walker, J.W., 2015. Seasonal trends in black carbon properties and co-pollutants in Mexico City. Atmos. Chem. Phys. 15, 12539-12582. https://doi.org/10.5194/acp-15-9693-2015

Rolph, G., Stein, A., Stunder, B., 2007. Real-time environmental applications and display system: Ready. Enivron. Modell. Softw. 95, 210-228. https://doi.org/10.1016/j.envsoft.2017.06.025

Sekiguchi, M., Nakajima, T., Suzuki, K., Kawamoto, K., Higurashi, A., Rosenfeld, D., Sano, I., Mukai, S., 2003. A study of the direct and indirect effects of aerosols using global satellite data sets of aerosol and cloud parameters. J.

Geophys. Res.-Atmos. 108 (D22), 4699. https://doi.org/10.1029/2002JD003359

Shi, G.L., Li, X., Feng, Y.C., Wang, Y.Q., Wu, J.H., Li, J., Zhu, T., 2009. Combined source apportionment, using positive matrix factorization–chemical mass balance and principal component analysis/multiple linear regression–chemical mass balance models. Atmos. Environ. 43, 2929-2937. https://doi.org/10.1016/j.atmosenv.2009.02.054

Sirois, A., Bottenheim, J.W., 1995. Use of backward trajectories to interpret the 5-year record of PAN and O_3 ambient air concentrations at Kejimkujik National Park, Nova Scotia. J. Geophys. Res.-Atmos. 100, 2867-2881. https://doi.org/10.1029/94JD02951

Song, Y., Zhang, Y., Xie, S., Zeng, L., Zheng, M., Salmon, L.G., Shao, M., Slanina, S., 2006. Source apportionment of $PM_{2.5}$ in Beijing by positive matrix factorization. Atmos. Environ. 40, 1526-1537. https://doi.org/10.1016/j.atmosenv.2005.10.039

Stein, A.F., Draxler, R.R., Rolph, G.D., Stunder, B.J.B., Cohen, M.D., Ngan, F., 2015. NOAA's HYSPLIT atmospheric transport and dispersion modeling system. Bull. Amer. Meteor. Soc. 96, 2059-2077. http://dx.doi.org/10.1175/BAMS-D-14-00110.1

Taghvaee, S., Sowlat, M.H., Mousavi, A., Hassanvand, M.S., Yunesian, M., Naddafi, K., Sioutas, C., 2018. Source apportionment of ambient $PM_{2.5}$ in two

locations in central Tehran using the Positive Matrix Factorization (PMF) model. Sci. Total Environ. 628-629, 672-686. https://doi.org/10.1016/j.scitotenv.2018.02.096

Takemura, T., Nozawa, T., Emori, S., Nakajima, T.Y., Nakajima, T., 2005. Simulation of climate response to aerosol direct and indirect effects with aerosol transport‐radiation model. J. Geophys. Res.-Atmos. 110, D02202. https://doi.org/10.1029/2004JD005029

Tao, J., Cheng, T.T., Zhang, R.J., 2012. Chemical composition of summertime $PM_{2.5}$ and its relationship to aerosol optical properties in Guangzhou, China. Atmos. Oceanic Sci. Lett. 5, 88-94. https://doi.org/10.1080/16742834.2012.11446971

Tao, J., Zhang, L., Cao, J., Hsu, S.C., Xia, X., Zhang, Z., Lin, Z., Cheng, T., Zhang, R., 2014a. Characterization and source apportionment of aerosol light extinction in Chengdu, southwest China. Atmos. Environ. 95, 552-562. https://doi.org/10.1016/j.atmosenv.2014.07.017

Tao, J., Zhang, L., Ho, K., Zhang, R., Lin, Z., Zhang, Z., Lin, M., Cao, J., Liu, S., Wang, G., 2014b. Impact of $PM_{2.5}$ chemical compositions on aerosol light scattering in Guangzhou — the largest megacity in South China. Atmos. Res. 135-136, 48-58. https://doi.org/10.1016/j.atmosres.2013.08.015

Turpin, B.J., Lim, H.J., 2001. Species contributions to $PM_{2.5}$ mass concentrations: revisiting common assumptions for estimating organic mass. Aerosol Sci. Technol. 35, 602-610. https://doi.org/ 10.1080/02786820119445

Viana, M., Rivas, I., Querol, X., Alastuey, A., Álvarez-Pedrerol, M., Bouso, L., Sioutas, C., Sunyer, J., 2015. Partitioning of trace elements and metals between quasi-ultrafine, accumulation and coarse aerosols in indoor and outdoor air in schools. Atmos. Environ. 106, 392-401. https://doi.org/10.1016/j.atmosenv.2014.07.027

Wang, G.H, Zhang, R.Y, Gomez M.E., Yang, L.X., Zamora, M.L., Hu, M., Lin, Y., Peng, J.F., Guo, S., Meng, J.J., Li, J.J., Cheng, C.L., Hu, T.F., Ren, Y.Q., Wang, Y.S., Gao, J., Cao. J.J., An, Z.S., Zhou, W.J., Li, G.H., Wang, J.Y., Tian, P.F., Marrero-Oriz, W., Secrest, J., Du, Z.F., Zheng, J., Shang, D.J., Zeng, L.M., Shao, M., Wang, W.G., Huang, Y., Wang, Y., Zhu, Y.J., Li, Y.X., Hu, J.X., Pan, B., Cai, L., Cheng, Y.T., Ji, Y.M., Zhang, F., Rosenfeld, D., Liss, P.S., Duce, R.A., Kolb, C.E., Molina, M.J., 2016a. Persistent sulfate formation from London Fog to Chinese haze. Proc. Natl. Acad. Sci. U. S. A. 113 (48), 13630-13635. https://doi.org/10.1073/pnas.1616540113

Wang, H., Shi, G., Tian, M., Zhang, L., Chen, Y., Yang, F., Cao, X., 2016b. Aerosol optical properties and chemical composition apportionment in Sichuan Basin, China. Sci. Total Environ. 577, 245-257. https://doi.org/10.1016/j.scitotenv.2016.10.173

Wang, J., Ho, S.S.H., Ma, S., Cao, J., Dai, W., Liu, S., Shen, Z., Huang, R., Wang, G., Han, Y., 2016c. Characterization of $PM_{2.5}$ in Guangzhou, China: uses of organic markers for supporting source apportionment. Sci. Total Environ. 550, 961-971. https://doi.org/10.1016/j.scitotenv.2016.01.138

Wang, J., Virkkula, A., Gao, Y., Lee, S., Shen, Y., Chi, X., Nie, W., Liu, Q., Xu, Z., Huang, X., Wang, T., Cui, L., Ding, A., 2017. Observations of aerosol optical properties at a coastal site in Hong Kong, South China. Atmos. Chem. Phys. 17, 2653-2671. https://doi.org/10.5194/acp-17-2653-2017

Wang, J., Zhang, Y.F., Feng, Y.C., Zheng, X.J., Jiao, L., Hong, S.M., Shen, J.D., Tan, Z., Ding, J., Zhang, Q., 2016d. Characterization and source apportionment of aerosol light extinction with a coupled model of CMB-IMPROVE in Hangzhou, Yangtze River Delta of China. Atmos. Res. 178-179, 570-579. https://doi.org/10.1016/j.atmosres.2016.05.009

Wang, P., Cao, J.J., Shen, Z.X., Han, Y.M., Lee, S.C., Huang, Y., Zhu, C.S., Wang, Q.Y., Xu, H.M., Huang, R.J., 2015a. Spatial and seasonal variations of $PM_{2.5}$ mass and species during 2010 in Xi'an, China. Sci. Total Environ. 508, 477-487. https://doi.org/10.1016/j.scitotenv.2014.11.007

Wang, Q., Cao, J., Han, Y., Tian, J., Zhu, C., Zhang, Y., Zhang, N., Shen, Z., Ni, H., Zhao, S., Wu, J., 2018. Sources and physicochemical characteristics of black carbon aerosol from the southeastern Tibetan Plateau: internal mixing

enhances light absorption. Atmos. Chem. Phys. 18, 4639-4656. https://doi.org/10.5194/acp-18-4639-2018

Wang, R., Tao, S., Shen, H., Wang, X., Li, B., Shen, G., Wang, B., Li, W., Liu, X., Huang, Y., Zhang, Y., Lu, Y., Ouyang, H., 2012. Global emission of black carbon from motor vehicles from 1960 to 2006. Environ. Sci. Technol. 46, 1278-1284. https://doi.org/10.1021/es2032218

Wang, Y.H., Liu, Z.R., Zhang, J.K., Hu, B., Ji, D.S., Yu, Y.C., Wang, Y.S., 2015b. Aerosol physicochemical properties and implications for visibility during an intense haze episode during winter in Beijing. Atmos. Chem. Phys. 15, 3205-3215. https://doi.org/10.5194/acp-15-3205-2015

Wang, Y.Q., Zhang, X.Y., Draxler, R.R., 2009. TrajStat: GIS-based software that uses various trajectory statistical analysis methods to identify potential sources from long-term air pollution measurement data. Environ. Modell. Softw. 24, 938-939. https://doi.org/10.1016/j.envsoft.2009.01.004

Watson, J.G., 2002. Visibility: science and regulation. J. Air Waste Manage. Assoc. 52, 628-713. https://doi.org/10.1080/10473289.2002.10470813

Xu, H.M., Cao, J.J., Ho, K.F., Ding, H., Han, Y.M., Wang, G.H., Chow, J.C., Watson, J.G., Khol, S.D., Qiang, J., Li, W.T., 2012a. Lead concentrations in fine particulate matter after the phasing out of leaded gasoline in Xi'an, China. Atmos. Environ. 46, 217-224. https://doi.org/10.1016/j.atmosenv.2011.09.078

Xu, J., Tao, J., Zhang, R., Cheng, T., Leng, C., Chen, J., Huang, G., Li, X., Zhu, Z., 2012b. Measurements of surface aerosol optical properties in winter of Shanghai. Atmos. Res. 109-110, 25-35. https://doi.org/10.1016/j.atmosres.2012.02.008

Zhang, Q., Streets, D.G., He, K.B., Wang, Y.X., Richter, A., Burrows, J.P., Uno, I., Jang, C.J., Chen, D., Yao, Z., Lei, Y., 2007. NO_x emission trends for China, 1995-2004: the view from the ground and the view from space. J. Geophys. Res. D. 112, D22306. https://doi.org/10.1029/2007JD008684

Zhang, R., Jing, J., Tao, J., Hsu, S.C., Wang, G., Cao, J., Lee, S.C., Zhu, L., Chen, Z., Zhao, Y., Shen, Z., 2013. Chemical characterization and source apportionment of $PM_{2.5}$ in Beijing: seasonal perspective. Atmos. Chem. Phys. 13, 7053-7074. https://doi.org/10.5194/acp-13-7053-2013

Zhang, T., Cao, J., Tie, X., Shen, Z., Liu, S., Ding, H., Han, Y., Wang, G., Ho, K.F., Qiang, J., Li, W.T., 2011. Water-soluble ions in atmospheric aerosols measured in Xi'an, China: seasonal variations and sources. Atmos. Res. 102, 110-119. https://doi.org/10.1016/j.atmosres.2011.06.014

Zhou, J., Ho, S.S.H., Cao, J., Zhao, Z., Zhao, S., Zhu, C., Wang, Q., Liu, S., Zhang, T., Zhao, Y., Wang, P., Tie, X., 2018. Chemical characterization of $PM_{2.5}$ from a southern coastal city of China: applications of modeling and chemical tracers in demonstration of regional transport. Environ. Sci. Pollut. Res. 25 (21), 20591-20605. https://doi.org/10.1007/s11356-018-2238-1

Zhou, Y., Wang, Q., Huang, R., Liu, S., Tie, X., Su, X., Niu, X., Zhao, Z., Ni, H., Wang, M., Zhang, Y., Cao, J., 2017. Optical properties of aerosols and implications for radiative effects in Beijing during the Asia-Pacific Economic Cooperation (APEC) Summit 2014. J. Geophys. Res.-Atmos. 122, 10119-10132. https://doi.org/10.1002/2017jd026997

Zhu, C.S., Cao, J.J., Ho, K.F., Chen, L-W.A., Huang, R.J., Wang, Y.C., Li, H., Shen, Z., Chow, J.C., Watson, J.G., Su, X.L., Wang, Q.Y., Xiao, S., 2015. The optical properties of urban aerosol in northern China: a case study at Xi'an. Atmos. Res. 160, 59-67. https://doi.org/10.1016/j.atmosres.2015.03.008

Figure captions:

Figure 1. Temporal variations of hourly (a) dry light scattering coefficient ($b_{scat,dry}$) and (b) light absorption coefficient (b_{abs}) during the whole sampling period.

Figure 2. Diurnal variations in (a) dry light scattering coefficient ($b_{scat,dry}$), (b) light absorption coefficient (b_{abs}), (c) wind speed, and (d) mixed layer depth averaged over the campaign. In each panel, the lower and upper edges of the boxes denote the 25% and 75% percentiles, respectively. The short black lines and pink circle inside the boxes indicate the median and mean values, respectively. The vertical bars ("whiskers") show the 10^{th} and 90^{th} percentiles. LST stands for local standard time.

Figure 3. Bivariate polar plots for dry light scattering coefficient ($b_{scat,dry}$) and light absorption coefficient (b_{abs}) based on wind speeds (ws, m s^{-1}) and directions during the daytime and the nighttime.

Figure 4. (a) Relationship between dry light extinction ($b_{ext,dry}$) reconstructed by the revised IMPROVE algorithm ($b_{ext,dry}$-reconstructed) and the one from PAX measurement ($b_{ext,dry}$, defined as the sum of $b_{scat,dry}$ and b_{abs}); (b) contributions of individual $PM_{2.5}$ chemical composition to $b_{ext,dry}$-reconstructed. $(NH_4)_2SO_4$, NH_4NO_3, OM, EC, SS, and FS represent ammonium sulfate, ammonium nitrate, organic matter, elemental carbon, sea salt, and fine soil, respectively.

Figure 5. Factor profiles for the six sources identified by the Hybrid Environmental Receptor Model (HERM).

Figure 6. (a) Relationship between dry light extinction ($b_{ext,dry}$) predicted by $PM_{2.5}$

source apportionment analysis ($b_{ext,dry}$-predicted) and the one from PAX measurement ($b_{ext,dry}$, defined as the sum of $b_{scat,dry}$ and b_{abs}); (b) contributions of each identified source to b_{ext}-predicted.

Figure 7. Source apportionment of aerosol optical properties at each three-day backward-trajectory cluster during the campaign period at Sanya. The numbers above the pie chart represent the average light extinction in the dry condition ($b_{ext,dry}$) for each cluster.

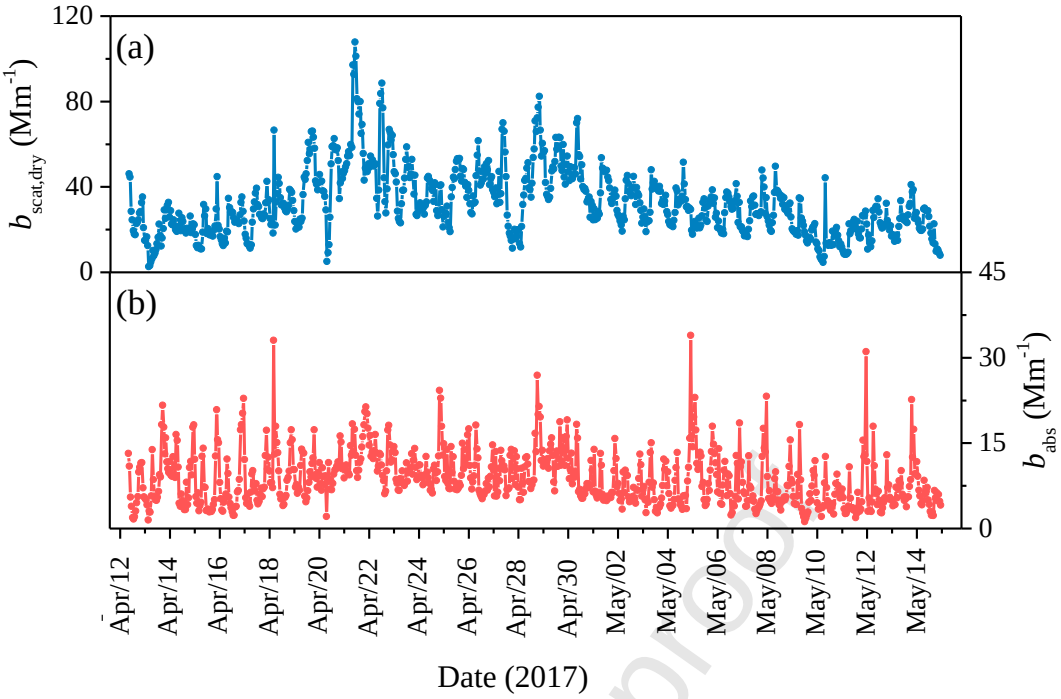

Figure 1. Temporal variations of hourly (a) dry light scattering coefficient ($b_{scat,dry}$) and (b) light absorption coefficient (b_{abs}) during the whole sampling period.

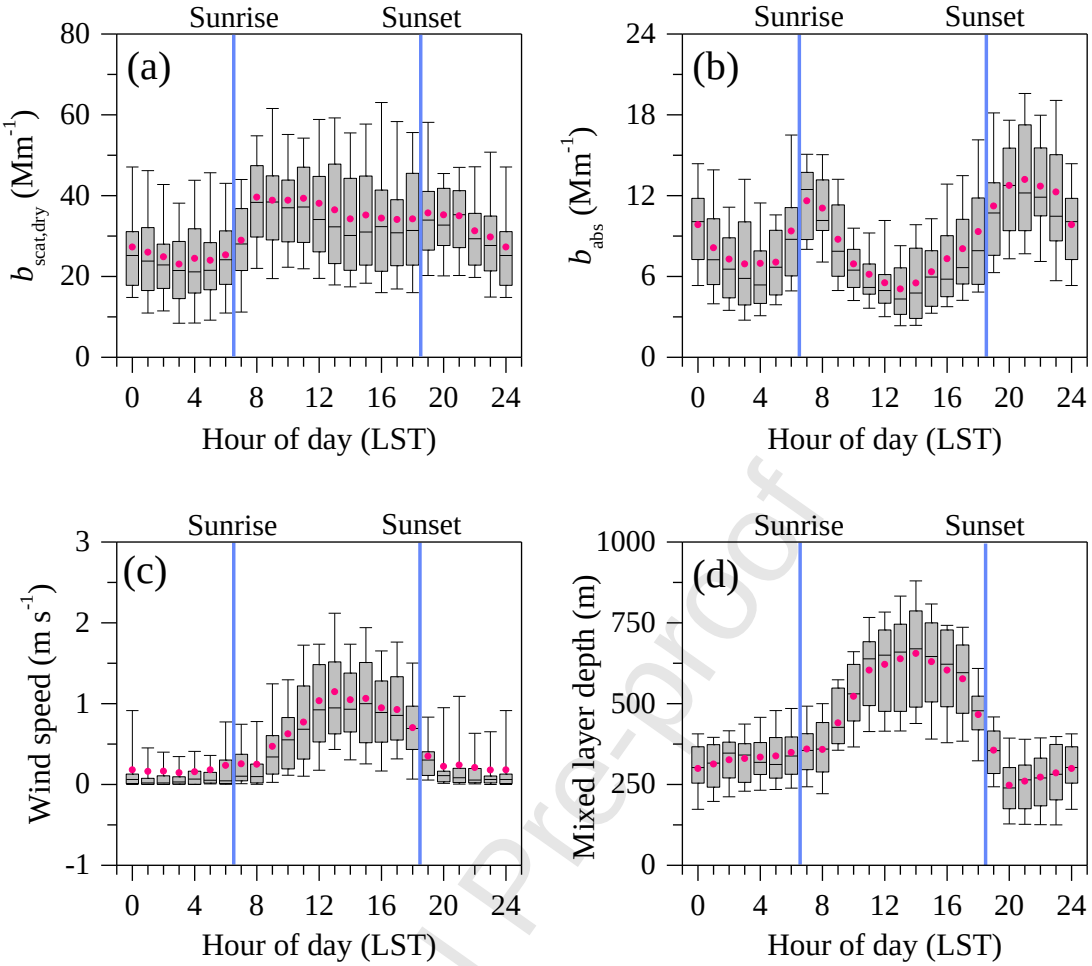

Figure 2. Diurnal variations in (a) dry light scattering coefficient ($b_{scat,dry}$), (b) light absorption coefficient (b_{abs}), (c) wind speed, and (d) mixed layer depth averaged over the campaign. In each panel, the lower and upper edges of the boxes denote the 25% and 75% percentiles, respectively. The short black lines and pink circle inside the boxes indicate the median and mean values, respectively. The vertical bars ("whiskers") show the 10th and 90th percentiles. LST stands for local standard time.

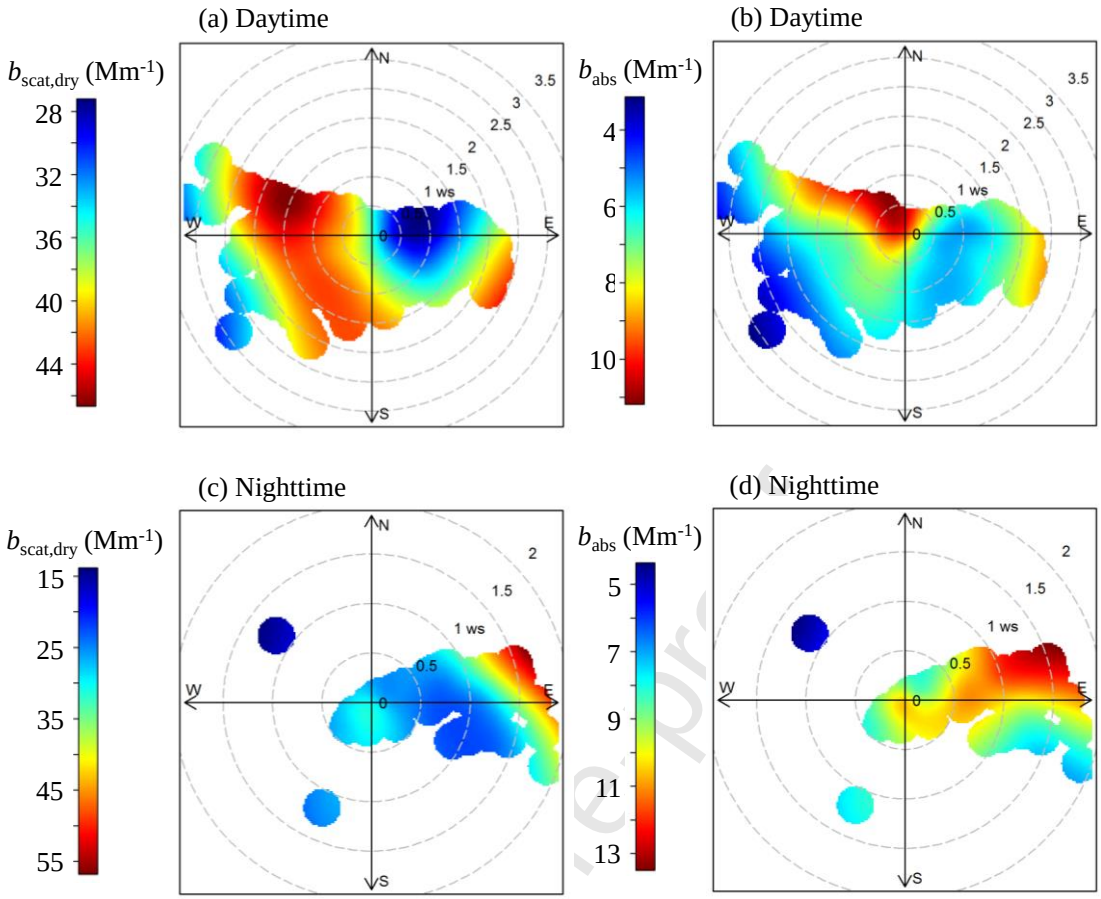

Figure 3. Bivariate polar plots for dry light scattering coefficient ($b_{scat,dry}$) and light absorption coefficient (b_{abs}) based on wind speeds (ws, m s^{-1}) and directions during the daytime and the nighttime.

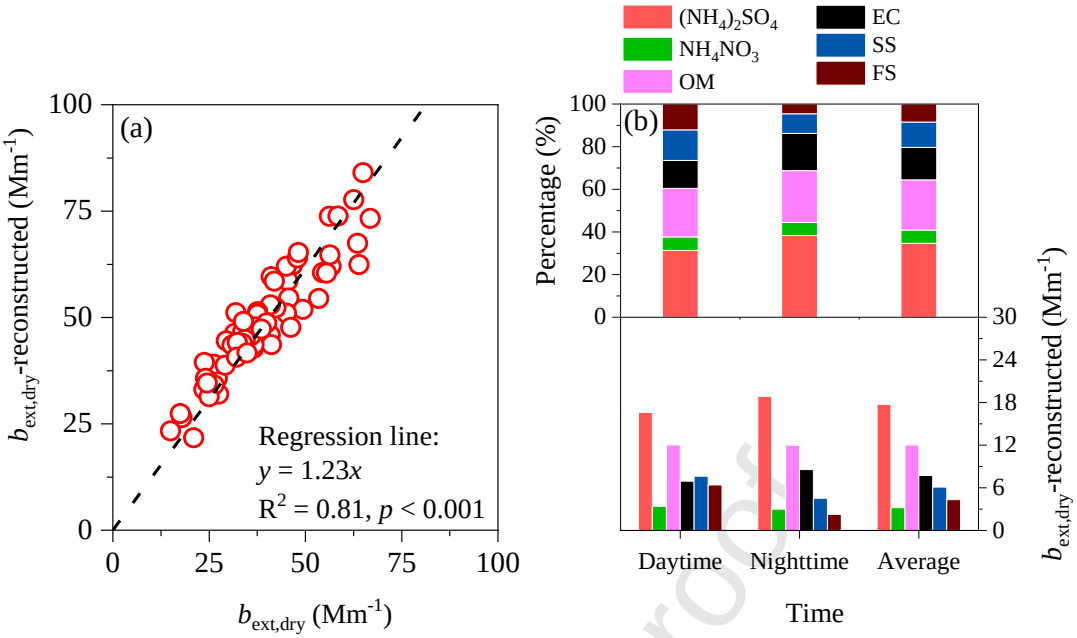

Figure 4. (a) Relationship between dry light extinction ($b_{ext,dry}$) reconstructed by the revised IMPROVE algorithm ($b_{ext,dry}$-reconstructed) and the one from PAX measurement ($b_{ext,dry}$, defined as the sum of $b_{scat,dry}$ and b_{abs}); (b) contributions of individual $PM_{2.5}$ chemical composition to $b_{ext,dry}$-reconstructed. $(NH_4)_2SO_4$, NH_4NO_3, OM, EC, SS, and FS represent ammonium sulfate, ammonium nitrate, organic matter, elemental carbon, sea salt, and fine soil, respectively.

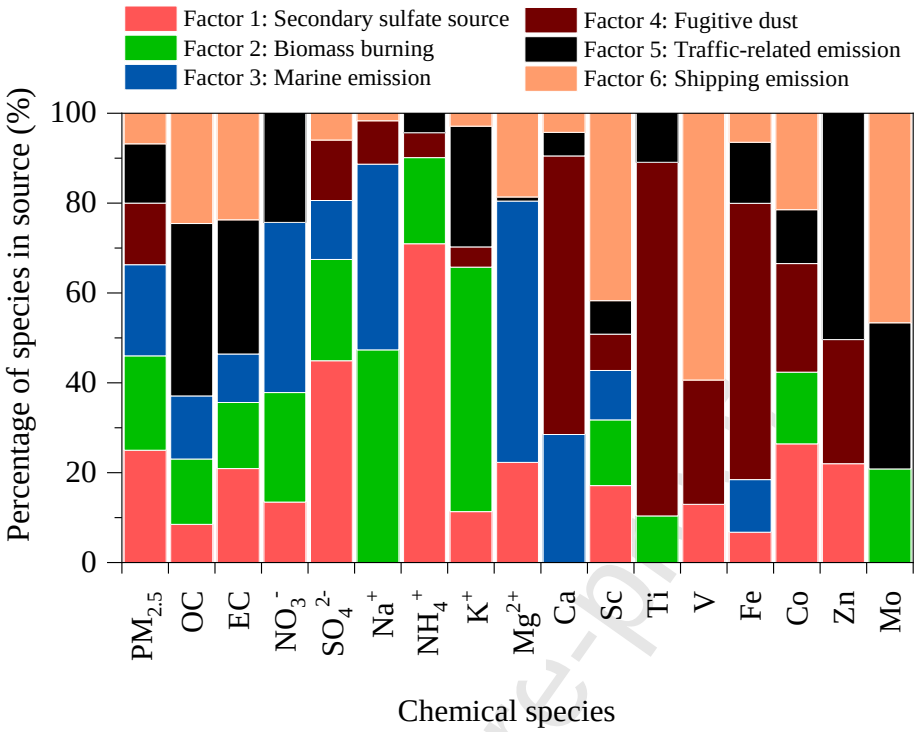

Figure 5. Factor profiles for the six sources identified by the Hybrid Environmental Receptor Model (HERM).

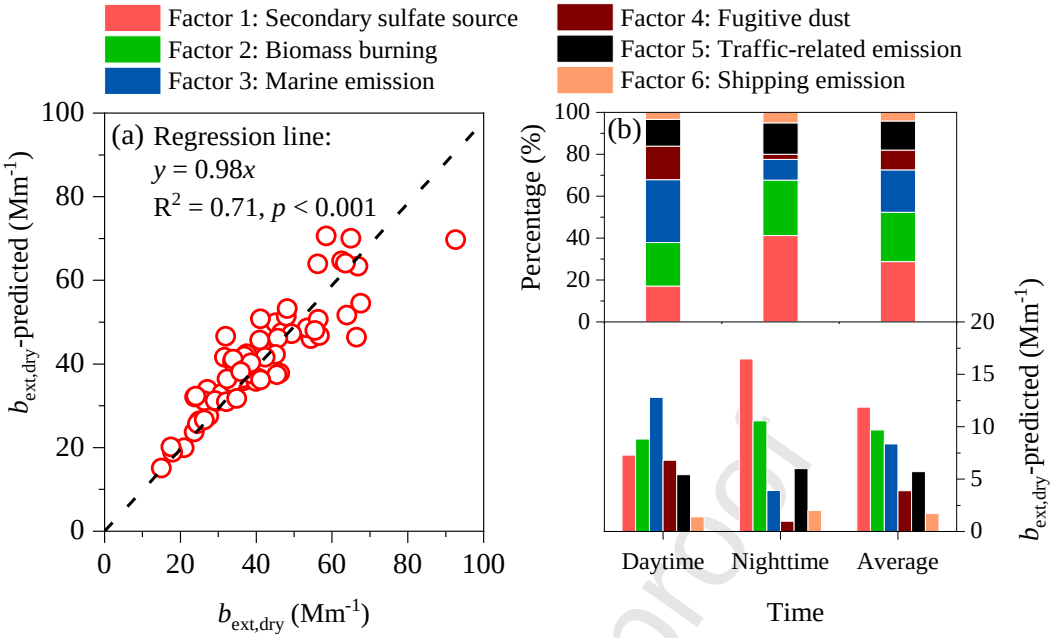

Figure 6. (a) Relationship between dry light extinction ($b_{ext,dry}$) predicted by $PM_{2.5}$ source apportionment analysis ($b_{ext,dry}$-predicted) and the one from PAX measurement ($b_{ext,dry}$, defined as the sum of $b_{scat,dry}$ and b_{abs}); (b) contributions of each identified source to $b_{ext,dry}$-predicted.

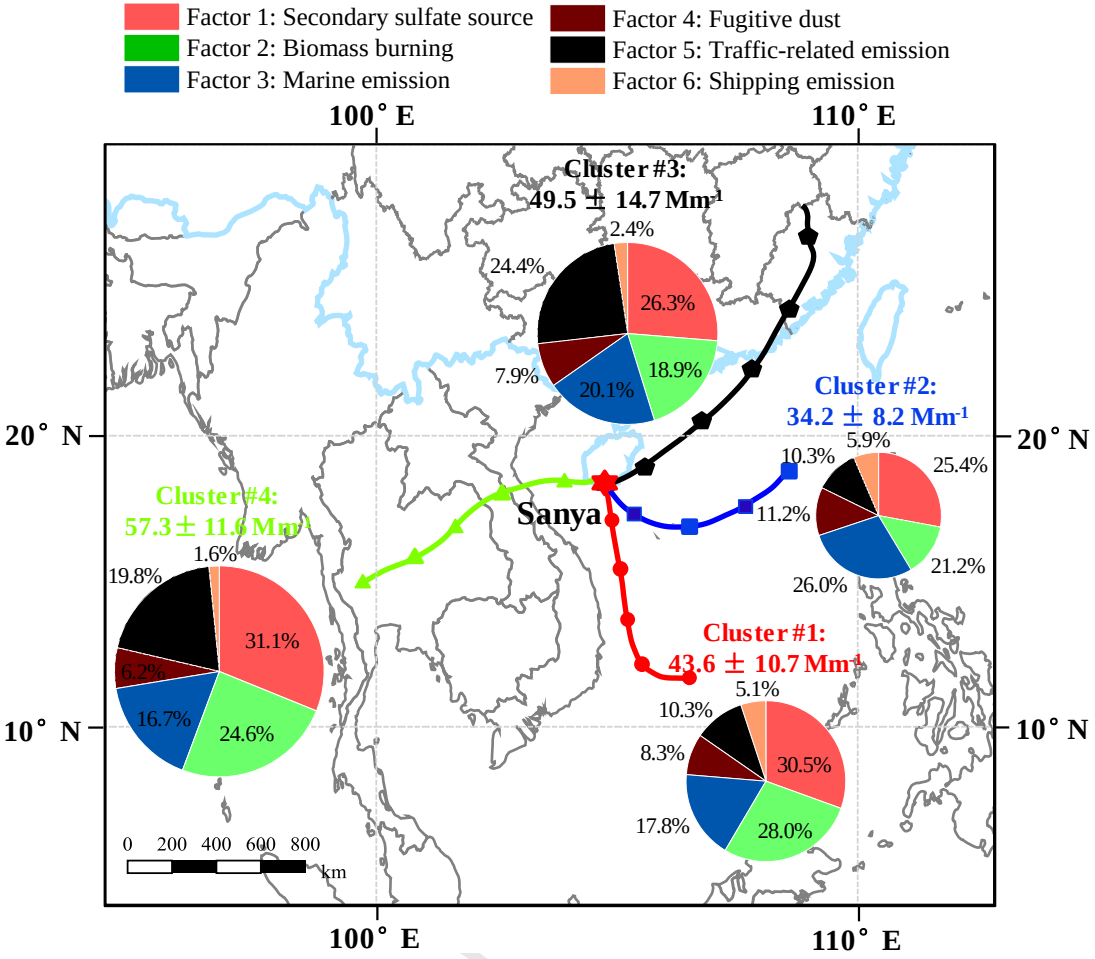

Figure 7. Source apportionment of aerosol optical properties at each three-day backward-trajectory cluster during the campaign period at Sanya. The numbers above the pie chart represent the average light extinction in the dry condition ($b_{ext,dry}$) for each cluster.

Table 1. Summary of dry light scattering coefficient ($b_{scat,dry}$) and light absorption coefficient (b_{abs}) as well as the concentrations of $PM_{2.5}$ and its chemical composition during the whole sampling period.

Component*	Daytime	Nighttime	Average
$b_{scat,dry}$ (Mm^{-1})	36.6 ± 16.6	28.3 ± 12.9	32.5 ± 15.5
b_{abs} (Mm^{-1})	7.6 ± 4.0	9.9 ± 5.0	8.8 ± 4.7
$PM_{2.5}$ ($\mu g\ m^{-3}$)	15.3 ± 3.7	13.4± 4.7	14.3 ± 4.2
EC ($\mu g\ m^{-3}$)	0.69 ± 0.24	0.86 ± 0.28	0.78 ± 0.27
OM ($\mu g\ m^{-3}$)	4.3 ± 1.7	4.3 ± 1.7	4.3 ± 1.7
$(NH_4)_2SO_4$ ($\mu g\ m^{-3}$)	4.5 ± 1.4	4.9 ± 1.8	4.7 ± 1.6
NH_4NO_3 ($\mu g\ m^{-3}$)	0.85 ± 0.29	0.72 ± 0.43	0.79 ± 0.37
FS ($\mu g\ m^{-3}$)	6.4 ± 2.3	2.3 ± 1.1	4.3 ± 2.7
SS ($\mu g\ m^{-3}$)	1.9 ± 0.6	1.1 ± 0.3	1.5 ± 0.6

* EC, OM, $(NH_4)_2SO_4$, NH_4NO_3, FS, and SS represent elemental carbon, organic matter, ammonium sulfate, ammonium nitrate, fine soil, and sea salt in $PM_{2.5}$, respectively.

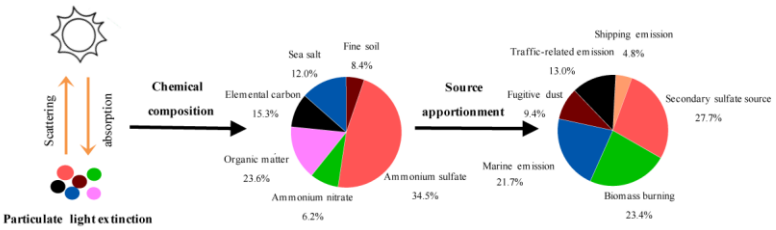

Graphical abstract

Highlights:

- The lower $b_{scat,dry}$ and b_{abs} were consistent with better air quality at Sanya.
- Ammonium sulfate and organic matter contributed most to $b_{ext,dry}$.
- Source contributions to $b_{ext,dry}$ changed from the daytime to the nighttime.
- Much higher contribution of biomass burning to $b_{ext,dry}$ was found from Southeast Asia.